Wind-reprocessed Transients

ANTHONY L. PIRO[1] AND WENBIN LU[2]

[1]*The Observatories of the Carnegie Institution for Science, 813 Santa Barbara St., Pasadena, CA 91101, USA; piro@carnegiescience.edu*

[2]*Theoretical Astrophysics, and Walter Burke Institute for Theoretical Physics, Mail Code 350-17, Caltech, Pasadena, CA 91125, USA; wenbinlu@caltech.edu*

ABSTRACT

We consider the situation where the luminosity from a transient event is reprocessed by an optically thick wind. Potential applications are the tidal disruption of stars by black holes, engine-powered supernovae, and unique fast transients found by current and future wide-field surveys. We derive relations between the injected and observed luminosity for steady and time dependent winds, and discuss how the temperature is set for scattering-dominated radiative transport. We apply this framework to specific examples of tidal disruption events and the formation of a black hole by a massive star, as well as discuss other applications such as deriving observables from detailed hydrodynamic simulations. We conclude by exploring what is inferred about the mass loss rate and underlying engine powering AT2018cow if it is explained as a wind-reprocessed transient, demonstrating that its optical emission is consistent with reprocessing of the observed soft X-rays.

*Keywords:* black hole physics — radiative transfer — supernovae: general

1. INTRODUCTION

With the growth of wide-field and high-cadence surveys in recent years (e.g., Brown et al. 2013; Shappee et al. 2014; Chambers et al. 2016; Tartaglia et al. 2018; Tonry et al. 2018; Graham et al. 2019), the study of astrophysical transients has literally exploded. This has led to increasingly detailed studies of well-known transients (e.g., thermonuclear and core-collapse supernovae, classical novae, and gamma-ray bursts) as well as the almost regular discovery and study of a vast range of new transients, including tidal disruption events (TDEs; Gezari et al. 2012; Holoien et al. 2014), kilonovae (Coulter et al. 2017), fast blue transients (FBOTs; Drout et al. 2014), calcium-rich transients (Kasliwal et al. 2012), fast radio bursts (FRBs; Lorimer et al. 2007; Thornton et al. 2013), and luminous red novae (Rau et al. 2007; Kasliwal et al. 2011; Williams et al. 2015), just to name a few.

These new events have in turn inspired astrophysicists to consider novel methods to power them, such as shock interaction (Balberg & Loeb 2011; Chevalier & Irwin 2011), fallback accretion (Dexter & Kasen 2013), radioactive heating from sources other than ^{56}Ni (Metzger et al. 2010), and spin down of highly-magnetized neutron stars (Kasen & Bildsten 2010). Besides the underlying energy source, a critical aspect for determining the observed properties of transients is the direct local environment around them. Perhaps no where is this better exemplified than with studies of interacting supernovae (e.g., Type IIn), where the properties can vary dramatically depending on the surrounding material

(e.g., Smith et al. 2007; Ofek et al. 2013), or TDEs, where the optical emission is likely the result of an underlying powering source being reprocessed (e.g., Strubbe & Quataert 2009; Miller 2015; Roth et al. 2016; Metzger & Stone 2016; Dai et al. 2018; Lu & Bonnerot 2020).

Motivated by these issues, we present a theoretical study of how the observed properties of a transient are altered when reprocessed by an outflow (or wind). Some of the basic framework for such a model was initially presented in the work of Strubbe & Quataert (2009) in the specific context of TDEs. Here we take a more general point of view so that in the future a broad range of powering sources and mass loss rates can be considered depending on the specific system of interest. Thus as new transients are discovered, the models here can help investigate whether a wind-reprocessed transient is a possible explanation, and if so, what it implies about the systems. Alternatively, this framework can be applied to specific theoretical models to make observational predictions. This could be especially useful as a way to post-process detailed hydrodynamic simulations to predict observables that would be too expensive to calculate using full radiative transfer.

In Section 2, we begin by considering the case of a steady (i.e., time-independent mass loading factor) wind. This helps provide some of the basic physical intuition for more complicated cases presented later. In Section 3, we consider how the situation is modified if the wind can now change with time. In Section 4, we investigate how the temperature of the reprocessed emission is expected to evolve, highlighting the importance of scattering-dominated radiative transport. In
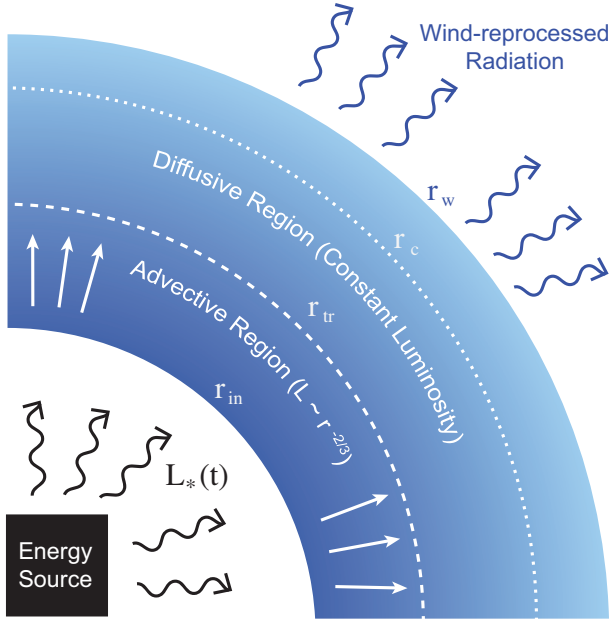
Figure 1. Diagram highlighting the key regions for a wind-reprocessed transient. An energy source (denoted by a black box) injects a luminosity $L_*(t)$, which heats a wind (denoted by the blue region) at a radius r_{in}. In the dense inner regions of the wind, this luminosity is advected along with the wind material out to the trapping radius r_{tr} (marked with a dashed line), above which the luminosity is roughly constant. Within this outer region, the outermost radius where thermalization can occur is at the color radius r_c (marked with a dotted line). The radii r_{tr} and r_c thus determine the luminosity and temperature, respectively, of the wind-reprocessed radiation seen by an observed.

Section 5, we consider toy models of TDEs and black hole (BH) formation in the context of our framework, and then in Section 6 we discuss what is implied about AT2018cow if it is explained as a wind-reprocessed transient. We conclude in Section 7 with a summary of our results and a discussion of future work.

2. STEADY WIND

For the basic setup, as shown in Figure 1, consider a luminosity L_* that is reprocessed by a steady, optically-thick wind with velocity v_w and mass-loss rate $\dot{M}$. The density profile of the wind is set by mass continuity to be

$$\rho(r) = \frac{\dot{M}}{4\pi r^2 v_w} = \frac{K}{r^2}, \tag{1}$$

where K is the mass-loading factor. The outer boundary of the wind evolves with time as

$$r_w = r_{in} + v_w t, \tag{2}$$

where r_{in} is the wind's inner boundary.

Given the temperatures and densities present for the scenarios we will be considering, the opacity of the wind is generally dominated by electron scattering $\kappa_s = 0.34\,\mathrm{cm^2\,g^{-1}}$ (for

a solar-like composition). Note that the absorption opacity is still important for determining the observed color temperature of the transient, which we address in more detail in Section 4. The scattering optical depth is given by

$$\tau(r) = \int_r^{r_w} \kappa_s \rho\, dr = \kappa_s K(r^{-1} - r_w^{-1}). \tag{3}$$

The photon diffusion time at a radius $r < r_w$ can be estimated as

$$t_{dif} \approx \frac{\tau(r)}{c} \frac{(r_w - r)r}{r_w}, \tag{4}$$

which matches the expected limits of $t_{dif} \approx (r_w - r)\tau/c$ when $r \approx r_w$ and $t_{dif} \approx r\tau/c$ when $r \ll r_w$. The dynamical time of a shell at radius r is

$$t_{dyn} \approx (r - r_{in})/v_w. \tag{5}$$

The photon trapping radius r_{tr} is defined as the depth where $t_{dif} = t_{dyn}$, which results in an algebraic expression

$$\frac{r_{tr}}{r_{in}} = 1 + \frac{\kappa_s K}{r_{in}} \frac{v_w}{c} \frac{(r_w - r_{tr})^2}{r_w^2} = 1 + A\frac{(r_w - r_{tr})^2}{r_w^2}. \tag{6}$$

The dimensionless constant

$$A \equiv \kappa_s K v_w / r_{in} c, \tag{7}$$

reflects how strongly radiation is trapped at the inner radius r_{in}. Thus, we require $A \gtrsim 1$, otherwise photons are never trapped. Equation (6) is quadratic in r_{tr}, and so it can be easily solved for given values of r_{in}, r_w, and A.

Photons injected at the inner radius r_{in} with luminosity L_* are advected along with the wind out to the trapping radius r_{tr}. This causes them to be adiabatically degraded, so that their energy density scales $\mathcal{E} \propto \rho^{4/3} \propto r^{-8/3}$ (Strubbe & Quataert 2009). Below the trapping depth the energy density is then

$$\mathcal{E}(r) = \frac{L_*}{4\pi r_{in}^2 v_w} \left(\frac{r}{r_{in}}\right)^{-8/3}. \tag{8}$$

Above the trapping depth, there is little adiabatic cooling and the luminosity is roughly constant. The observed luminosity is set by the flux of radiation across the trapping depth

$$L_{obs} = 4\pi r_{tr}^2 \mathcal{E}(r_{tr}) \left(v_w - \frac{dr_{tr}}{dt}\right), \tag{9}$$

where note we have been careful to include the effect of the changing trapping depth (reflected in the dr_{tr}/dt term) that is often not included in other similar analytic treatments. Thus, the ratio between the observed and injected luminosities is

$$\frac{L_{obs}}{L_*} = \left(\frac{r_{tr}}{r_{in}}\right)^{-2/3} \left(1 - \frac{1}{v_w}\frac{dr_{tr}}{dt}\right), \tag{10}$$

Combining Equations (6) and (10) provides the full time evolution of the observed luminosity. We next analytically estimate the evolution of the ratio L_{obs}/L_* at different characteristic times during the expansion of the wind.

2.1. Early Times

The ratio of the wind expansion to its initial radius gives a dimensionless measure of the time $v_w t / r_{\rm in}$. For $v_w t / r_{\rm in} \ll 1$, the wind has not expanded appreciably and $r_{\rm tr} \approx r_w \sim r_{\rm in}$. Evaluating Equation (6) in this limit,

$$(r_w - r_{\rm tr})^2 = \frac{r_w^2}{A} \frac{r_{\rm tr} - r_{\rm in}}{r_{\rm in}} \approx \frac{r_w^2}{A} \frac{r_w - r_{\rm in}}{r_{\rm in}} = \frac{r_w^2 v_w t}{A r_{\rm in}}. \quad (11)$$

Taking the square root of this expression and then the time derivative, we obtain

$$1 - \frac{1}{v_w} \frac{d r_{\rm tr}}{dt} \approx \frac{1}{2} \left(\frac{r_w^2}{A r_{\rm in} v_w t} \right)^{1/2}. \quad (12)$$

Substituting this into Equation (10),

$$\frac{L_{\rm obs}}{L_*} \approx \frac{1}{2} \left(\frac{r_{\rm tr}}{r_{\rm in}} \right)^{-2/3} \left(\frac{r_w}{A r_{\rm in}} \right)^{1/2} \left(\frac{r_w}{v_w t} \right)^{1/2}. \quad (13)$$

Thus as sufficiently early times $L_{\rm obs}/L_* \propto t^{-1/2}$.

2.2. Middle Times

Next, for $v_w t / r_{\rm in} \gg 1$, then $r_{\rm tr} \approx r_w \approx v_w t \gg r_{\rm in}$, and from Equation (6) we find,

$$(r_w - r_{\rm tr})^2 = \frac{r_w^2}{A} \frac{r_{\rm tr} - r_{\rm in}}{r_{\rm in}} \approx \frac{r_w^3}{A r_{\rm in}} \approx \frac{v_w^3 t^3}{A r_{\rm in}}. \quad (14)$$

Again taking the square root of this expression and then the time derivative,

$$1 - \frac{1}{v_w} \frac{d r_{\rm tr}}{dt} \approx \frac{3}{2} \left(\frac{v_w t}{A r_{\rm in}} \right)^{1/2}. \quad (15)$$

so that

$$\frac{L_{\rm obs}}{L_*} \approx \frac{3}{2} \left(\frac{r_{\rm tr}}{r_{\rm in}} \right)^{-2/3} \left(\frac{v_w t}{A r_{\rm in}} \right)^{1/2}. \quad (16)$$

Now that $r_{\rm rt} \approx v_w t$, then $L_{\rm obs}/L_* \propto t^{-2/3} t^{1/2} \propto t^{-1/6}$.

2.3. Late Times

Eventually, $v_w t / r_{\rm in} \gg A$, so that $r_w \gg r_{\rm tr} \gg r_{\rm in}$. In this case Equation (6) can be used to show $r_{\rm tr} \approx A r_{\rm in}$, which is constant with time. Thus $1 - v_w^{-1} d r_{\rm tr}/dt \approx 1$. This is equivalent to taking $\tau(r_{\rm tr}) \approx c/v_w$, which is the classic condition typically used for the trapping radius (e.g., Strubbe & Quataert 2009). Here we see that this is only valid when the wind has expanded sufficiently away from the trapping radius, and that the solution to Equation (6) should be used in general. In this case,

$$\frac{L_{\rm obs}}{L_*} \approx A^{-2/3}, \quad (17)$$

which is just a fixed ratio with time as long as A is constant (we consider an evolving A in Section 3).
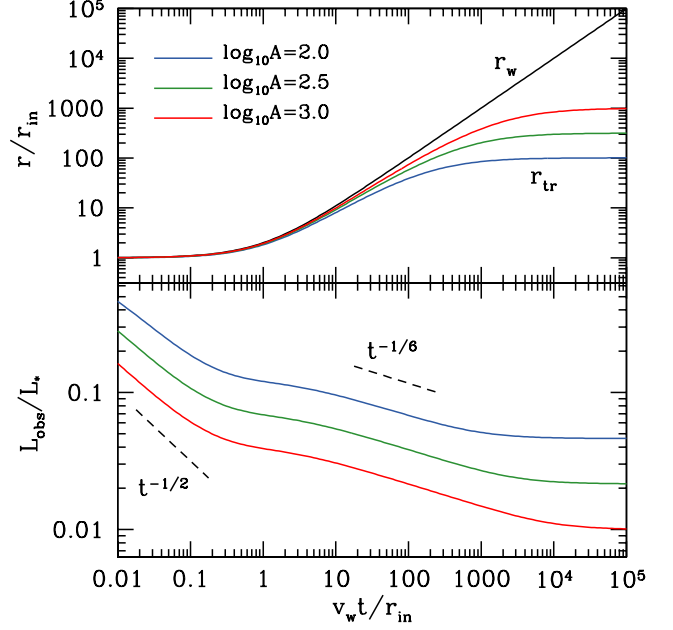
Figure 2. Radius and luminosity evolution for a steady wind. The upper panel plots the wind radius r_w (black line) and the trapping radius $r_{\rm tr}$, which is solved from Equation (6), for different values of A as indicated. The trapping radius evolution shows distinct changes at $v_w t / r_{\rm in} \approx 1$ and $v_w t / r_{\rm in} \approx A$, which correspond to breaks between the early, middle, and late stages. The bottom panel plots the observed luminosity ratio using Equation (10). This exhibits power-law evolution as derived in the text.

2.4. Full Solutions for Steady Wind

Full solutions for the evolution of a steady wind are plotted in Figure 2 for different values of A. This shows the expected features estimated analytically in the previous sections. The trapping radius initially evolves along with r_w, but then asymptotes to $r_{\rm tr}/r_{\rm in} \approx A$ once $v_w t / r_{\rm in} \gg A$. The luminosity evolves from $L_{\rm obs} \propto t^{-1/2}$ to $L_{\rm obs} \propto t^{-1/6}$ before finally asymptoting to $L_{\rm obs}/L_* = A^{-2/3}$.

We caution though that some of the features of this evolution are more for academic interest. Early on the wind may require a timescale $\sim r_{\rm in}/v_w$ to develop. Furthermore, there may be a timescale associated with actually generating the illuminating luminosity. For these reasons, there will likely be a rise to peak that is not resolved in the treatment here.

3. EVOLVING WIND

In general, one might expect the mass loss of the wind to evolve, so we next consider the more general case where the mass loading parameter K is a function of time.

3.1. Basic Framework

We assume that the velocity of the wind keeps a characteristic constant value v_w. If a shell is launched into the wind at a radius $r_{\rm in}$ and at a time t_0, then it reaches a radius r at a

time

$$t = t_0 + (r - r_{\rm in})/v_w. \qquad (18)$$

This means that if we want the density profile at any time t, then it is given by

$$\rho(r,t) = K[t_0(r,t)]/r^2, \qquad (19)$$

and the optical depth at any time and radius is

$$\tau(r,t) = \int_r^{r_w} \kappa_s \rho(r,t) dr = \kappa_s \int_r^{r_w} \frac{K[t_0(r,t)]}{r^2} dr. \qquad (20)$$

The trapping radius is found by equating the diffusion and dynamical times

$$\frac{\tau(r_{\rm tr})}{c} \frac{(r_w - r_{\rm tr})r_{\rm tr}}{r_w} = t - t_0. \qquad (21)$$

The observed luminosity is

$$L_{\rm obs}(t) = L_*[t_0(r_{\rm tr},t)] \left[\frac{r_{\rm tr}(t)}{r_{\rm in}}\right]^{-2/3} \left(1 - \frac{1}{v_w}\frac{dr_{\rm tr}}{dt}\right), \qquad (22)$$

where we note one must be careful to evaluate the injected luminosity L_* at the injection timescale t_0 for the current trapping radius.

3.2. *Power-Law Wind Evolution*

To provide more intuition about how the an evolving wind differs from a steady wind, it is helpful to consider some toy models. In the simplest physically-motivated cases, such as winds driven from a disk or fallback in a tidal disruption event, the wind-loading factor scales as a power law with time with the form

$$K(t) = K_{\rm max}(1 + t/t')^{-\beta}, \qquad (23)$$

where $K_{\rm max}$ is the maximum wind-loading factor, t' is the timescale for the wind to begin changing, and a typical value for the power law is $\beta \approx 5/3$ (other values such as $\beta = 4/3$ may be considered for a wind driven from a radiatively inefficient disk). Rewritten in dimensionless terms, the wind loading can be expressed as

$$A(t) = A_{\rm max}(1 + t/t')^{-\beta} \qquad (24)$$

where $A_{\rm max} \equiv \kappa_s K_{\rm max} v_w/r_{\rm in}c$. The introduction of the additional timescale t', in comparison to the previously discussed timescale $r_{\rm in}/v_w$, results in a richer diversity of evolution for $L_{\rm obs}/L_*$.

We next solve the set of equations described above for power-law wind evolution. Here we just summarize how solutions for a time-dependent wind differ from a steady one. Readers interested in the specific techniques we employ to calculate these solutions should consult Appendix A.
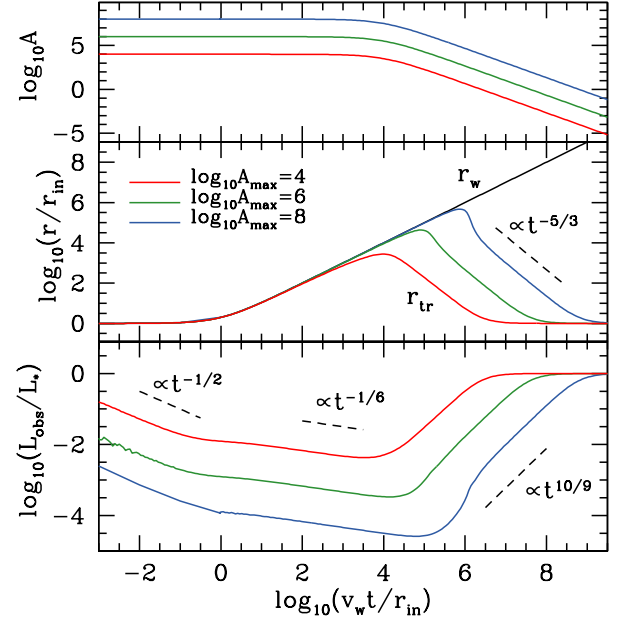
Figure 3. The evolution for $v_w t'/r_{\rm in} = 10^4$ and $\beta = 5/3$ with different values of $A_{\rm max}$ as denoted. For $t < t'$, the wind is constant and mostly matches our steady wind solutions. For $t > t'$, the wind mass loss decreases and $r_{\rm tr}$ and $L_{\rm obs}$ follow the power law evolution given by Equations (25) and (26), respectively.

First, in Figure 3 we consider how the solutions evolve with different values of $A_{\rm max}$ and the dimensionless wind time is relatively large in comparison to unity with $v_w t'/r_{\rm in} = 10^4$. For times $t < t'$, the wind is roughly constant and the evolution goes through two stages that roughly mimic what we found before for the steady wind case. Namely, initially the trapping radius is roughly constant with $L_{\rm obs}/L_* \propto t^{-1/2}$ and next $r_{\rm tr} \approx r_w \propto t$ with $L_{\rm obs}/L_* \propto t^{-1/6}$.

For times $t > t'$, the wind is changing with $A(t) \approx A_{\rm max}(t/t')^{-\beta}$. Using the late time solutions from Section 2.3, the trapping radius then evolves as

$$r_{\rm tr} \approx A r_{\rm in} \approx A_{\rm max} r_{\rm in}(t/t')^{-\beta}, \qquad (25)$$

and the observed luminosity as

$$L_{\rm obs}/L_* \approx A^{-2/3} \approx A_{\rm max}^{-2/3}(t/t')^{2\beta/3}. \qquad (26)$$

Both scalings match what we find numerically for $\beta = 5/3$. Note though that the changes in the evolution of $r_{\rm tr}$ and $L_{\rm obs}$ happen later than the change in A. This is because if the wind evolution changes at a time t' then the trapping radius and luminosity only react at a later time of $\approx t' + (r_{\rm tr} - r_w)/v_w$. Eventually $r_{\rm tr} \approx r_{\rm in}$ and stops evolving with $L_{\rm obs} \approx L_*$. This happens when

$$t > t' A_{\rm max}^{1/\beta}. \qquad (27)$$

This occurs later for larger t' and $A_{\rm max}$ as also shown by the numerical solutions.
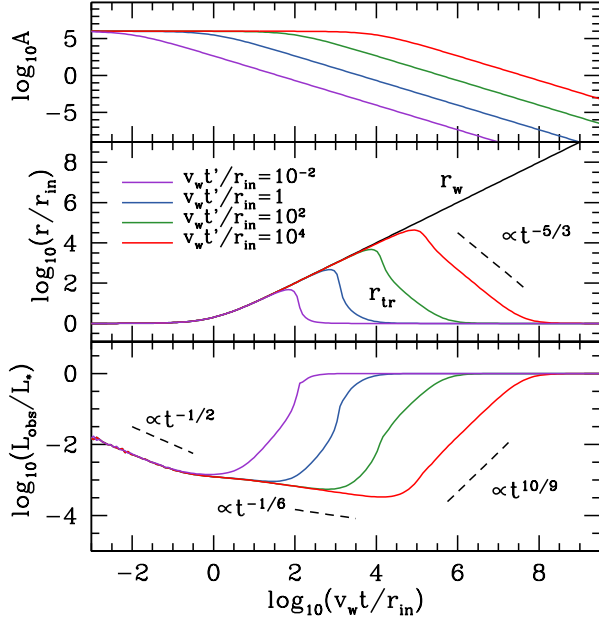
Figure 4. The evolution when we fix $A_{max} = 10^6$ and $\beta = 5/3$ and vary t'. For large values of t', the evolution matches what was found in Figure 3. As we decrease t', the intermediate stage (where $r_{tr} \approx r_w$ and $L_{obs}/L_* \propto t^{-1/6}$) gets shorter and shorter. Finally, for $v_w t'/r_{in} \lesssim 1$ (purple line), the luminosity transitions directly between early and late phases.

In Figure 4, we now fix $A_{max} = 10^6$ and instead vary the value of t'. When $v_w t'/r_{in} \gg 1$, then the evolution matches what was found above. For smaller values of t', the solutions transition sooner to the phase where the trapping radius is moving back into the wind. Note though that because the solutions also transition sooner to $r_{tr} \approx r_{in}$, the power laws of $r_{tr} \propto t^{-\beta}$ and $L_{obs}/L_* \propto t^{2\beta/3}$ are not obeyed as closely. Thus we expect in practice that when t' is small it will be more difficult to infer exactly what β is from the observed time evolution.

3.3. *Summary for Evolving Wind*

To summarize the results of this section, the scalings we expect for the trapping radius and observed luminosity are

$$r_{tr}/r_{in} \propto \begin{cases} 1, & t \lesssim r_{in}/v_w \\ t, & r_{in}/v_w \lesssim t \lesssim t' \\ A(t), & t' \lesssim t \lesssim t' A_{max}^{1/\beta} \\ 1, & t \gtrsim t' A_{max}^{1/\beta}. \end{cases} \quad (28)$$

and

$$L_{obs}/L_* \propto \begin{cases} t^{-1/2}, & t \lesssim r_{in}/v_w \\ t^{-1/6}, & r_{in}/v_w \lesssim t \lesssim t' \\ A(t)^{-2/3}, & t' \lesssim t \lesssim t' A_{max}^{1/\beta} \\ 1, & t \gtrsim t' A_{max}^{1/\beta}, \end{cases} \quad (29)$$

respectively. When $t' \lesssim r_{in}/v_w$ (as in the blue and purple solutions in Figure 4) the second phase may be skipped entirely. Note that the timescales for each of these phases is approximate because of the time it takes to get to r_{tr} after the wind is launched, but this gives a sense of the scalings expected.

4. TEMPERATURE EVOLUTION

The above sections focus on the evolution of the luminosity of a wind-reprocessed transient, but another important observable is the temperature. At any depth the temperature is dominated by radiation so that

$$aT(r,t)^4 = \mathcal{E}(r,t), \quad (30)$$

where a is the radiation constant. Below the trapping radius, this is set by the adiabatic cooling, so that

$$T(r,t) = \left(\frac{L_*[t_0(r,t)]}{4\pi r_{in} v_w a} \right)^{1/4} \left(\frac{r}{r_{in}} \right)^{-2/3}. \quad (31)$$

Above the trapping radius, the luminosity is constant with depth. The energy density and temperature are then determined according to flux limited diffusion

$$L_{obs}(t) = -\frac{4\pi r^2 ac}{3\kappa_s \rho[t_0(r,t)]} \frac{\partial T(r,t)^4}{\partial r}. \quad (32)$$

In practice, we simplify Equation (32) when solving for the temperature distribution by dropping the dr_{tr}/dt in L_{obs}. With the exception of the earliest rising phases, this introduces a less than 5% error on L_{obs} and an even smaller error on the temperature estimate. Furthermore, we can solve Equation (32) analytically if we take $t_0 \approx t$, resulting in

$$T(r,t) \approx \left[\frac{\kappa_s K(t) L_{obs}(t)}{4\pi r^3 ac} \right]^{1/4}. \quad (33)$$

Although this can provide a reasonable approximation for the temperature profile as long as K is not changing too quickly with time, for the numerical examples considered later we solve Equation (32) exactly.

If we set $\tau \approx 1$ using Equations (3) or (20), we can solve for the electron scattering photosphere. In general though, the effective temperature measured at this radius does not correspond to the observed color temperature. This is because the opacity for absorption is lower than that of electron scattering which dominates the wind. Thermalization requires that the wind is sufficiently optically thick that photon absorption can take place (also see the discussion in Shen et al. 2015). For an absorptive opacity $\kappa_a \ll \kappa_s$, we can define an effective opacity (Rybicki & Lightman 1986)

$$\kappa_{eff} = (3\kappa_s \kappa_a)^{1/2}, \quad (34)$$

and an associated effective optical depth

$$\tau_{eff} = \int_r^{r_w} \kappa_{eff} \rho dr, \quad (35)$$

where we note that κ_a (and in turn κ_{eff}) can be a function of the density and temperature in the wind. The condition $\tau_{eff} \approx 1$ defines the color radius r_c. In general, r_c can either be above or below r_{tr}, so we next consider the resulting observed color temperature T_{obs} for each of these cases.

4.1. Trapping-dominated Temperature

First, consider the case where $r_c < r_{tr}$ (note this is different than shown in Figure 1, where the trapping radius is interior to the color radius). In this instance, the photons are thermally coupled to the wind material out to the radius r_c, but then continue to be adiabatically cooled out to the radius r_{tr} due to advection. This means that the energy density of photons effectively evolves with depth as if they are coupled, until reaching the radius r_{tr} above which the photons diffuse out with few absorptions. Thus the observed temperature matches Equation (31) evaluated at r_{tr},

$$T_{obs}(t) = \left(\frac{L_*[t_0(r_{tr}, t)]}{4\pi r_{in}^2 v_w a} \right)^{1/4} \left(\frac{r_{tr}(t)}{r_{in}} \right)^{-2/3}. \quad (36)$$

Again, if we ignore the factor of dr_{tr}/dt for L_{obs}, this can be rewritten as

$$T_{obs} \approx \left(\frac{L_{obs}}{4\pi r_{tr}^2 v_w a} \right)^{1/4}. \quad (37)$$

For different stages of the evolution, the temperature will roughly scale as

$$T_{obs} \propto \begin{cases} L_*(t)^{1/4} t^{-1/8}, & t \lesssim r_{in}/v_w \\ L_*(t)^{1/4} t^{-13/24}, & r_{in}/v_w \lesssim t \lesssim t' \\ L_*(t)^{1/4} A(t)^{-5/8}, & t' \lesssim t \lesssim t' A_{max}^{1/\beta}. \end{cases} \quad (38)$$

At sufficiently late times when $t \gtrsim t' A_{max}^{1/\beta}$, the photons may not be able to thermalize at all and the observed temperature may better reflect the spectrum the photons were injected with.

4.2. Thermalization-dominated Temperature

The other case is when $r_c > r_{tr}$ (as shown in Figure 1). This is expected to occur for denser winds. Now even once the photons are no longer advected with the flow, they will continue to be thermalized with the wind material. The energy density of this material is set solving Equation (32), so that

$$T_{obs}(t)^4 \approx - \int_{r_c(t)}^{r_w(t)} \frac{3\kappa_s K[t_0(r,t)] L_{obs}(t)}{4\pi r^4 ac} dr. \quad (39)$$

For this case, it is more difficult to derive general scalings with time because r_c will be evolving with time in a way that depends on the exact functional form of κ_a. This motivates us to consider some more specific examples in the next section.

5. SPECIFIC EXAMPLES

Since r_c can evolve in more complicated ways than just simple scalings, here we consider some specific examples to better understand how the evolution proceeds. We still stick with power law scalings for both $L_*(t)$ and $K(t)$, namely

$$L_*(t) = L_{max}(1 + t/t')^{-\alpha}, \quad (40)$$

and Equation (23) for $K(t)$. Different physical scenarios will result in different values of L_{max}, K_{max}, t', α, and β as described next.

Furthermore, we need to consider a specific form for κ_a for these calculations. The absorptive opacity can be a complicated function of density and temperature depending on the relative important of bound-bound, bound-free, and free-free interactions. For illustrative purposes, here we use a Kramer's opacity

$$\kappa_a = \kappa_0 \rho T^{-3.5} \, cm^2 \, g^{-1}. \quad (41)$$

For the specific examples below, we use $\kappa_0 = 2 \times 10^{24}$ (assuming ρ and T are in cgs units), which is meant to mimic a bound-free opacity for roughly solar composition (Hansen & Kawaler 1994). In more detailed calculations, other opacity forms or tabulated opacities can be used. Although a helpful simplification is that as long as $r_c < r_{tr}$, then the observed temperature no longer depends on the exact value of κ_a as.

We note that in the following Sections 5.1 and 5.2, we mostly summarize the main features of the solutions. The details of how we solve the system of equations for the radius, luminosity, and temperature evolution are presented in Appendix A and B.

5.1. Tidal Disruption Events

For the first example, we consider the tidal disruption event (TDE) of a solar mass star by a supermassive black hole. There remains considerable uncertainty in where the powering originates from in such events, whether it be from a small amount of material fed into the BH (Metzger & Stone 2016), dissipation of stream self-interaction (Piran et al. 2015), or secondary shocks (Bonnerot & Lu 2019). In any scenario though it is generally thought that there is reprocessing of the emission from these sites because of the relatively low temperatures ($\sim 10^4$ K) measured from observations in comparison to what is expected from the emission regions ($\gtrsim 10^5$ K).

For the disruption of a star with mass M_* and radius R_* by a black hole with mass M_{BH}, the fallback of material falling a tidal disruption event scales roughly as

$$\dot{M}_{fb} = \dot{M}_{max}(1 + t/t_{fb})^{-5/3}, \quad (42)$$

where

$$t_{fb} \approx 41 \left(\frac{M_{BH}}{10^6 M_\odot} \right)^{1/2} \left(\frac{M_*}{M_\odot} \right)^{-1} \left(\frac{R_*}{R_\odot} \right)^{3/2} \, days, \quad (43)$$
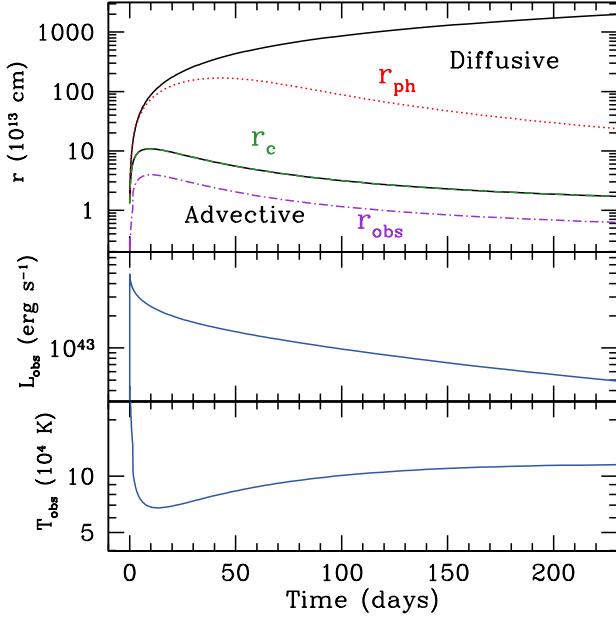
Figure 5. Evolution of the TDE of an $M_* = M_\odot$ star by an $M_{\rm BH} = 10^6 M_\odot$ using the framework developed here. For the injected luminosity we set $\eta = 10^{-3}$. In the top panel, the upper black line is r_w and the lower black line is $r_{\rm tr}$. These divide the diffusive and advective regions of the flow as labeled. The other key lines are the scattering photosphere $r_{\rm ph}$ (dotted red line), the radius where the temperature is determined r_c (dashed green line), and inferred observed radius (dot-dashed purple line). The color depth is always below the trapping radius in this case and thus the temperature is determined at the trapping radius. The middle and bottom panels show the observed bolometric luminosity and temperature, respectively.

and

$$\dot{M}_{\rm max} = \frac{M_*}{3t_{\rm fb}}$$
$$\approx 2.9 \left(\frac{M_{\rm BH}}{10^6 M_\odot}\right)^{-1/2} \left(\frac{M_*}{M_\odot}\right)^2 \left(\frac{R_*}{R_\odot}\right)^{-3/2} M_\odot \, {\rm yr}^{-1}.$$
$$(44)$$

If this material is radiatively inefficient as it tries to accrete, only a fraction η of this material can radiate its energy while the remaining energy goes into driving a wind. We follow Metzger & Stone (2016) and assume $\eta \ll 1$, which is also empirically supported by observed TDEs. We then take

$$L_* = \eta \dot{M}_{\rm fb} c^2, \qquad (45)$$

and $K \approx \dot{M}_{\rm fb}/4\pi v_w$ with $v_w \approx 10^9 \, {\rm cm \, s}^{-1}$ motivated by both observations of TDEs and theoretical expectations for the escape velocity. For the inner radius, we use $r_{\rm in} \approx 100 r_g$, where $r_g = GM_{\rm BH}/c^2 = 1.5 \times 10^{11}(M_{\rm BH}/10^6 M_\odot)\,{\rm cm}$.

An example solution is presented in Figure 5. In addition to the other key radii that are described above, we also plot

the scattering photosphere $r_{\rm ph}(t)$, defined as

$$\tau[r_{\rm ph}(t)] = \int_{r_{\rm ph}(t)}^{r_w} \frac{\kappa_s K[t_0(r,t)]}{r^2} dr = 1, \qquad (46)$$

and the observationally inferred radius, defined as

$$r_{\rm obs} \equiv \left(\frac{L_{\rm obs}}{4\pi\sigma_{\rm SB}T_{\rm obs}^4}\right)^{1/2}. \qquad (47)$$

This latter radius is what an observer would infer from assuming that the TDE emission is simply black body. We can see that this is actually much smaller than any of the other key radii associated with this event, because the thermalization is so weak in the outer layers of the wind (due to $\kappa_a \ll \kappa_s$). The rise-segment of the lightcurve (for $t \lesssim t_{\rm fb}$) should be smoother if a more realistic fallback rate from simulations is adopted (e.g., Lodato et al. 2009; Guillochon & Ramirez-Ruiz 2013).

This general framework is able to replicate the main features of TDEs, namely, a photosphere that recedes with time, a falling luminosity in the range of $\sim 10^{43}$–$10^{44} \, {\rm erg \, s}^{-1}$, and a roughly constant temperature in the range of $\sim 10^4$–10^5 K. Our model mostly follows the results of Metzger & Stone (2016), but with a detailed consideration of what sets the color temperature. Roth et al. (2016) nicely present through analytic and numerical arguments where the color temperature is set (referred to as the "optical continuum photosphere" in this work), but our study differs in that we follow the trapping radius. Since we find that the color depth is below the trapping depth for this toy model, this conveniently means that the details of κ_a do not matter as much for setting the observed temperature. However, if one includes a detailed treatment of bound-free and bound-bound absorption (with appropriate line broadening), the color depth may be above the trapping depth, and in that case, the observed color temperature is lower than obtained here (Lu & Bonnerot 2020).

This model demonstrates that the photosphere inferred via observations (e.g., Holoien et al. 2016) and fitting techniques (e.g., Mockler et al. 2019) that assume black body emission are not fitting for the true emission radius because the wind is highly scattering dominated. Making the approximation that $r_{\rm tr} \ll r_w$ and that $K(t)$ is not changing too quickly with time, we can estimate

$$r_{\rm obs} \approx \left(\frac{4v_w}{c}\right)^{1/2} r_{\rm tr} \approx \left(\frac{4v_w}{c}\right)^{1/2} \frac{\kappa_s \dot{M}}{4\pi c}. \qquad (48)$$

Thus one may be able to use this inferred radius to learn more about the wind surrounding the event.

5.2. Stellar Mass Black Hole Formation

The second example we consider is the fallback of material onto a newly born black hole following unsuccessful core collapse, similar to the scenario envisioned by
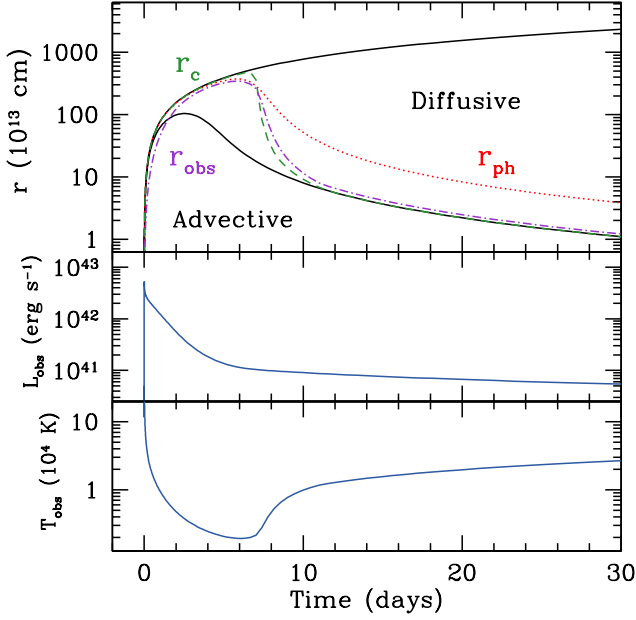
Figure 6. The same as Figure 5, but for a stellar mass BH form-ing event. Here, initially r_c is beyond the trapping radius, but then becomes equal to r_{tr} at $\sim 10\,$days.

Kashiyama & Quataert (2015). The basic picture is of a massive star that collapses in a failed supernova to become a black hole. With sufficient angular momentum, the fallback material produces an accretion disk around the newly born black hole. Such disks generally produce super-Eddington accretion rates which drive strong disk winds. Accretion onto the black hole illuminates these winds, leading to a fast blue transient.

In this case, we again expect that the fallback rate scales as $t^{-5/3}$ as shown in the work of Dexter & Kasen (2013). The relevant timescale is now the fallback time or

$$t_{fb} \approx \pi (R_*^3/8GM_{BH})^{1/2}$$
$$\approx 7 \left(\frac{M_{BH}}{7M_\odot}\right)^{-1/2} \left(\frac{R_*}{10R_\odot}\right)^{3/2} \mathrm{hr}, \qquad (49)$$

where we use a BH mass similar to the peak of the galactic black hole mass distribution (Özel et al. 2010) and a radius that would be appropriate for a Wolf-Rayet or blue supergiant star. The corresponding accretion rate for a disk with mass M_d can be estimated as

$$\dot{M}_d \approx M_d/t_{fb}$$
$$\approx 5 \times 10^{-5} \left(\frac{M_d}{M_\odot}\right) \left(\frac{M_{BH}}{7M_\odot}\right)^{1/2} \left(\frac{R_*}{10R_\odot}\right)^{-3/2} M_\odot\,\mathrm{s}^{-1}.$$
$$(50)$$

For simplicity, we assume that the fallback is the rate limiting step for feeding the BH, rather than the viscous time of the

disk. This is supported by simulations of accretion of low angular gas (e.g., Proga & Begelman 2003a,b), but in future work one could also track the viscous evolution of the disk including a fallback term using a simple disk model to better track the time dependent accretion rate (e.g., Metzger et al. 2008).

Since this accretion rate is orders of magnitude greater than the Eddington accretion rate for this black hole, we again assume that the majority of this mass is blown in a wind while merely a fraction $\eta \ll 1$ is accreted by the BH just as in our consideration of TDEs. The typical launching radius of this wind is the characteristic radius of the disk, which depends on the angular momentum of the star. Since this can vary depending on the mass loss history of a given star, we parameterize this radius with the factor f_d, so that

$$r_d \approx \frac{2GM_{BH}}{c^2} f_d \approx 2 \times 10^7 \left(\frac{f_d}{10}\right) \left(\frac{M_{BH}}{7M_\odot}\right) \mathrm{cm}. \quad (51)$$

This implies a relatively high launching velocity,

$$v_w \approx \left(\frac{2GM_{BH}}{r_d}\right)^{1/2} \approx 0.3 \left(\frac{f_d}{10}\right)^{-1/2} c. \quad (52)$$

As in the TDE case, we assume that a fraction of the material η is able to accrete onto the newly born BH, which produces a luminosity of $L_d \approx \eta \dot{M}_d c^2$ that illuminates these winds.

The resulting luminosity evolution is shown in Figure 6, where we have used the above parameters along with $\eta = 10^{-2}$ (see Appendix A for more details about these solutions). The main difference in comparison to the TDE case is that the winds are now much denser due to the high $\dot{M}_d$. This causes the color radius to be above the trapping radius at early times (the case described in Section 4.2). Nevertheless, the general observed features are largely similar, with an inferred emission radius that moves to smaller radii and a rather constant or slightly increasing observed temperature. The photospheric radius evolution we find is qualitatively different from the models studied by Kashiyama & Quataert (2015). In their case, the accretion onto the BH dramatically drops once the stellar surface falls in. This results in ejecta concentrated in a narrow radius and a photosphere that moves outward. Here we use a fallback rate that falls as $t^{-5/3}$ at late times. Such a scaling is applicable to a scenario where a low energy explosion expands the star but is ultimately unsuccessful in unbinding it (e.g., Dexter & Kasen 2013).

5.3. *Other Scenarios*

The above examples are meant to provide some sense of the range of systems that can be addressed with the framework presented here. There are many other scenarios where this work could be applied in future investigations.

Wind Collision. One example would be the collision of a wind with circumstellar material (CSM). As the wind with

mass loss rate $\dot{M}$ collides with the CSM, some fraction η of its kinetic energy would be converted to a luminosity $L_* = \eta \dot{M} v_w^2 / 2$. Here η roughly corresponds to the fraction of solid angle subtended by the CSM. As the collision occurs, the shocked wind moves more slowly than that unimpeded wind. The radiation produced in the shocked regions must then diffuse through the unimpeded wind to get to the observer. Although our framework is one-dimensional, it would still be fairly accurate for this case as long as the majority of the wind gets past the CSM and the emission is not too viewing angle dependent.

Magnetar Formation. Another possible scenario is the formation of a highly magnetized neutron star (magnetar). The basic picture is that following the merger of two neutron stars, it is likely in many cases that the result will either be a neutron star or at least a remnant that can hold off collapsing to a BH for a short while due to its high spin. The strong differential rotation of this process can generate large magnetic field ($B \gtrsim 10^{15}$ G; Price & Rosswog 2006; Zrake & MacFadyen 2013; Duncan & Thompson 1992), which produces a high luminosity of $\sim 10^{48}$ erg s^{-1} from the spin down. At the same time, this remnant would be surrounded by a $\sim 0.1 M_\odot$ disk of material that produces winds through its low radiative efficiency and heating via neutrinos. Such a scenario has been considered for a magnatar with supernova-like ejecta (Metzger & Piro 2014), but the emission may be qualitatively different if the environment was dominated by winds (e.g., Dessart et al. 2009; Fernández & Metzger 2013).

Nuclear Heating. Finally, another energy source we have not considered in the above examples is nuclear heating. In cases were a white dwarf explosion does not successfully unbind the star, the remnant may produce winds driven by leftover radioactive material (Shen & Schwab 2017). Applying this framework to such a scenario may help to better understand the Type Iax supernovae (Foley et al. 2013) that have been hypothesized to be these failed explosions (Foley et al. 2014). Although at sufficiently late times, these winds may be cool enough to produce dust (Fox et al. 2016; Foley et al. 2016), which is not accounted for in this work.

6. INTERPRETING AT2018COW

The fast, blue transient AT2018cow (Prentice et al. 2018; Ho et al. 2019) showed a power-law declining luminosity, a receding inferred photosphere, roughly thermal spectra, and radio/X-ray emission indicative of some sort of underlying power source. Despite extensive multiband observations of this event (Kuin et al. 2019; Margutti et al. 2019; Perley et al. 2019; Prentice et al. 2018; Ho et al. 2019; Rivera Sandoval et al. 2018), there is no agreed upon explanation for its origin, with ideas including a TDE by an intermediate mass BH (Perley et al. 2019), collapse of a massive

star to produce a BH (Quataert et al. 2019), magnetar creation (Margutti et al. 2019), electron capture of a merged white dwarf (Lyutikov & Toonen 2019), shocked disk interaction buried within a supernova (Margutti et al. 2019), and a common envelope with jets (Soker et al. 2019). Nevertheless, many of these features show similarities to what we would expect for a wind-reprocessed transient, in particular the declining radius. Whether or not this is the ultimate explanation for AT2018cow, we can at least investigate what our model would imply about the physical parameters associated with this transient.

If we assume that AT2018cow follows the case where the temperature is determined at the trapping radius, we use Equation (48) to estimate the wind mass loss rate at any give time

$$\dot{M} \approx \frac{4\pi c r_{\rm obs}}{\kappa_s} \left(\frac{4 v_w}{c} \right)^{1/2}. \qquad (53)$$

This ignores the time it takes to travel from the inner to the trapping radius, but this is at least good enough to get a rough idea of what $\dot{M}$ should be. Next, the observed optical luminosity and radius can be used to estimate what underlying luminosity was injected into the wind

$$L_* \approx L_{\rm obs} \left(\frac{r_{\rm tr}}{r_{\rm in}} \right)^{2/3} \approx L_{\rm obs} \left(\frac{r_{\rm obs}}{r_{\rm in}} \right)^{2/3} \left(\frac{c}{4 v_w} \right)^{1/3}. \quad (54)$$

Given $L_{\rm obs}$ and $r_{\rm obs}$ from the observations, we can derive what L_* and $\dot{M}$ should be. The only unknowns are v_w and $r_{\rm in}$.

Figure 7 shows the results of this analysis for $v_w = 0.1c$ and $r_{\rm in} = 10^{14}$ cm. The wind velocity is motivated by the rapid rise of the optically inferred photospheric radius in the first few days (Perley et al. 2019), as well as the shock speed inferred from the evolution of the flux at the synchrotron self-absorption frequency (Ho et al. 2019). The upper panel shows the inferred $\dot{M}$ (red circles), which shows a wind loss rate in the range of $\dot{M} \approx 10^{-8} - 10^{-6} M_\odot$ s^{-1} with a broken power-law evolution. The range of power laws that fit the late time $\dot{M}$ evolution are suggestive of a wind, either in the case of radiatively inefficient disk wind ($\dot{M} \sim t^{-4/3}$) or fallback accretion that is blown into a wind ($\dot{M} \sim t^{-5/3}$).

The middle panel shows the inferred L_* (blue squares). In comparison, we include the soft $(0.3 - 10 \text{keV})$ X-ray luminosity observed (black line; Margutti et al. 2019). The similarity of the inferred injection luminosity L_* and the rough time evolution of the X-rays (if the X-rays are considered in a time-averaged sense) supports the suggestion of Margutti et al. (2019) that the soft X-rays are reprocessed to produce the optical emission. The normalization of L_* does depend on the chosen value of $r_{\rm in}$, but this comparison shows that $r_{\rm in} \approx 10^{14}$ cm gives a reasonable explanation for this event. At early times, L_* is much greater than the observed X-ray luminosity. This is consistent with the idea of
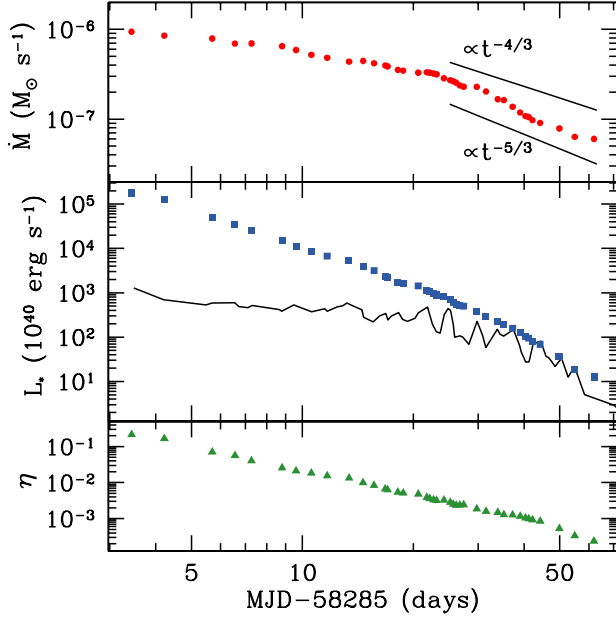
Figure 7. Inferred $\dot{M}$ (red circles) and L_* (blue squares) for AT2018cow, assuming that it is wind-reprocessed with $v_w = 0.1c$ and $r_{in} = 10^{14}$ cm. The bottom panel plots $\eta = L_*/(\dot{M}v_w^2/2)$ (green triangles), the efficiency inferred assuming that the powering luminosity is related to the wind mass loss rate. The late time mass rate asymptotes to a power law. An index in the range of $\approx -4/3$ to $-5/3$ suggests that a disk wind or fallback scenario could explain this reprocessing material. At late times, L_* is similar to the observed X-ray luminosity L_X (black line; Margutti et al. 2019), suggesting that the optical emission results from these reprocessed X-rays. At early times $L_* > L_X$, which is expected if the X-rays are highly obscured. The efficiency η is required to be $\approx 0.1 - 0.2$ early on and falls to $\lesssim 10^{-3}$ after about 50 days. We discuss potential reasons for this behavior in the text.

Margutti et al. (2019) that the X-rays are initially partially obscured but then mostly observed at later times.

In the lower panel of Figure 7, we plot the inferred efficiency $\eta = L_*/(\dot{M}v_w^2/2)$ (green triangles) under the assumption that the wind mass loss rate is connected to the powering luminosity. This connection is not in general required because L_* could be from some underlying engine, but it is interesting to consider η and what it might imply about AT2018cow. We see that $\eta \approx 0.1$ at early times and drops to below $\approx 10^{-3}$ at late times. The decrease of η is intriguing and we offer two speculations for this behavior. One possibility is that the X-rays are produced by a wind interacting with an equatorial torus of material. As the torus is eroded (only the densest clumps survives the shocks at late time), the efficiency of converting the kinetic energy of the wind into X-rays decreases. A second possibility is that v_w is not constant as assumed and is instead dropping with time. In the case of a viscously spreading disk (a compact inner disk), v_w will decrease as the disk radius increases according to the

local escape speed. Future more detailed modeling is needed to determine if either of these scenarios are possible or if another explanation could explain for these trends we infer.

7. CONCLUSIONS AND DISCUSSION

We considered the general properties of a transient that is being reprocessed by an optically thick wind. We separately studied the cases of a steady wind and a wind that is changing with time. We discussed how these winds will likely be scattering dominated and explore how this impacts the observed temperature evolution. This framework is applied to two specific cases, TDEs (where A_{max} is small and t' is large) and stellar mass BH formation (where A_{max} is large and t' is small) to provide more concrete examples of how reprocessing can work.

Given a $K(t)$ and $L_*(t)$ for some specific scenario, the methods presented in Section 3 can be used to solve for observed luminosity. A wide range of different potential applications are described in Section 5, and even among these there are different variations that would be interesting to explore. This framework may be especially helpful when evaluating numerical models where the hydrodynamics are solved for but the radiative transfer is not included because it is deemed too expensive. This can be done by using the numerical output to find $K(t)$ and $L_*(t)$ and then solving the equations presented in Section 3.1 numerically (including tabulated κ_a and κ_s).

Finally, we discussed the transient AT2018cow in the context of a wind-reprocessed framework. At a basic level, this example provides a template for how to approach other transients in the future and assess whether a wind-reprocessed model is applicable. One can use Equations (53) and (54) to estimate the evolution of $\dot{M}$ and L_* needed to make a wind-reprocessed model work. These in turn can be used to judge whether such a model is physically reasonable.

An important diagnostic which indicates that such a model should be considered is *an inward propagating radius.* This is a classic property of TDEs and also something that made AT2018cow stand out in comparison to many other transients. Unfortunately, for many of the interesting fast transients that have been discovered the radius evolution has not been followed (e.g., Ho et al. 2020), but it should be a priority to measure this property in the future. A decreasing radius has even been inferred for some seemingly normal core-collapse SNe (e.g., SN 2018bbc, Karamehmetoglu et al. 2019), suggesting broader application of this model.

Applying this model to AT2018cow, the two main conclusions were that (1) the $\dot{M}$ evolves as a power law, which is suggestive of a disk-wind or fallback scenario, and (2) that L_* is similar to the X-rays observed from AT2018cow, which fits with a picture where these X-rays are reprocessed to produce the optical emission. Beyond these basic properties,

the wind-reprocessed model for AT2018cow is fairly agnostic to the details of the source of the X-rays, but it is interesting to speculate. The time dependence of L_* is much steeper than would be expected for millisecond magnetar spin down (which would give $L_* \sim t^{-2}$) or fallback from a TDE ($L_* \sim t^{-5/3}$). This makes it difficult to explain with such a picture unless the efficiency for producing the X-ray emission is changing dramatically with time.

Perhaps more attractive is X-rays produced from shock interaction as described by Margutti et al. (2019) or even by Andrews & Smith (2018) in the context of iPFT14hls. In this picture, a centrally launched wind interacts with pre-explosion equatorial material (similar to the ejecta-equatorial ring interaction in SN 1987A), producing the observed X-rays. The rough scale of $r_{in} \sim 10^{14}$ cm needed for L_* to be comparable to the observed X-ray luminosity should depend on the conditions of the pre-existing equatorial material and should be checked against expectations for equatorial outflows before explosion. The variability of the X-rays would naturally be explained by interaction with clumps of matter, which would be more difficult to understand in models where the powering is more like an engine. The winds would originate from a long-lived disk accreting onto the central compact object and have a time dependence dictated by either fallback material or radiatively inefficient viscous evolution.

More work should be done to understand the three dimensional structure of wind material in AT2018cow. This is outside the scope of this current work since our main goal is to present the basic framework of wind-reprocessed transients. Nevertheless, given the mass loss rates estimated here, one should check whether the X-ray evolution (both in soft and hard bands) makes sense. Such an investigation would help constrain the covering fraction of the equatorial material and the viewing angle of the observer. It would also hopefully provide a better understanding of the stellar progenitor required to make AT2018cow.

APPENDIX

A. NUMERICALLY SOLVING FOR AN EVOLVING WIND

Here we derive the equations for an evolving wind using dimensionless variables to help with finding numerical solutions. First, we define dimensionless radial and time variables

$$\chi \equiv r/r_{in}, \quad \xi \equiv v_w t/r_{in}. \tag{A1}$$

Then the relation for the launching time from Equation (18) becomes

$$\xi = \xi_0 + \chi - 1, \tag{A2}$$

where $\xi_0 = v_w t_0 / r_{in}$. We define a new optical depth

$$\tilde{\tau}(\chi, \xi) = \tau(r, t) v_w / c = \int_\chi^{\chi_w} \frac{A[\xi_0(\chi, \xi)]}{\chi^2} d\chi, \tag{A3}$$

where

$$\chi_w = 1 + \xi, \tag{A4}$$

and the dimensionless wind parameter is

$$A(\xi) \equiv \kappa_s K(\xi) v_w / r_{in} c. \tag{A5}$$

The condition for finding the trapping radius given by Equation (21) is simplified to be

$$\tilde{\tau}(\chi_{tr}, \xi) \chi_{tr} (1 + \xi - \chi_{tr}) = \chi_w (\xi - \xi_0). \tag{A6}$$

From here we find χ_{tr} for a given ξ via iteration. The steps are as follows. (1) A trial χ_{tr} is chosen between 1 and χ_w. (2) We integrate Equation (A3) to find $\tilde{\tau}(\chi_{tr}, \xi)$. (3) This is substituted into Equation (A6). (4) If the left-hand side is too big, then we need to choose a smaller χ_{tr}, and the converse if the left-hand side is too small. With a new trial χ_{tr}, we go back to step (2) until we have converged on the correct value of χ_{tr}. Once the trapping radius is found, we use

$$L_{obs}(\xi) = L_*(\xi_0) \chi_{tr}^{-2/3} \left(1 - \frac{d\chi_{tr}}{d\xi} \right), \tag{A7}$$

to find the observed luminosity as a function of time.

B. DIMENSIONLESS VARIABLES FOR SPECIFIC EXAMPLES

For the cases where the wind loss rate is evolving with time as a power law as considered in Sections 3.2 and 5, we use a dimensionless wind parameter

$$A(\xi) = A_{\max}(1 + \xi/\xi')^{-\beta}, \tag{B8}$$

where $\xi' \equiv v_w t'/r_{\rm in}$. If we set $L_* = \eta \dot{M} c^2$, L_* in terms of A is

$$L_* = 4\pi r_{\rm in} \eta A c^3 / \kappa_s. \tag{B9}$$

For a TDE as discussed in Section 5.1,

$$A_{\max} = \frac{\kappa_s \dot{M}_{\max}}{4\pi r_{\rm in} c} = 16.7 \left(\frac{M_{\rm BH}}{10^6 M_\odot}\right)^{-1/2} \left(\frac{M_*}{M_\odot}\right)^2 \left(\frac{R_*}{R_\odot}\right)^{-3/2} \left(\frac{r_{\rm in}}{10^{13}\,{\rm cm}}\right)^{-1}, \tag{B10}$$

and

$$\xi' = \frac{v_w t_{\rm fb}}{r_{\rm in}} = 3.5 \times 10^2 \left(\frac{M_{\rm BH}}{10^6 M_\odot}\right)^{1/2} \left(\frac{M_*}{M_\odot}\right)^{-1} \left(\frac{R_*}{R_\odot}\right)^{3/2} \left(\frac{v_w}{10^9\,{\rm cm\,s^{-1}}}\right) \left(\frac{r_{\rm in}}{10^{13}\,{\rm cm}}\right)^{-1}. \tag{B11}$$

For fallback stellar mass BH formation event as discussed in Section 5.2, we take $r_{\rm in} \approx r_d$, so that

$$A_{\max} = \frac{\kappa_s \dot{M}_d}{4\pi r_d c} = 1.3 \times 10^9 \left(\frac{f_d}{10}\right)^{-1} \left(\frac{M_d}{M_\odot}\right) \left(\frac{M_{\rm BH}}{7 M_\odot}\right)^{-1/2} \left(\frac{R_*}{10 R_\odot}\right)^{-3/2}, \tag{B12}$$

where we use $\kappa_s \approx 0.1\,{\rm cm^2\,g^{-1}}$, as would be appropriate for partially ionized hydrogen-deficient material, and

$$\xi' = \frac{v_w t_{\rm fb}}{r_d} = 1.1 \times 10^7 \left(\frac{f_d}{10}\right)^{-3/2} \left(\frac{M_{\rm BH}}{7 M_\odot}\right)^{-3/2} \left(\frac{R_*}{10 R_\odot}\right)^{3/2}. \tag{B13}$$

Thus the TDE and BH formation cases span the parameter range from low to high values of $A_{\max}$ and ξ'.

REFERENCES

Andrews, J. E., & Smith, N. 2018, MNRAS, 477, 74

Balberg, S., & Loeb, A. 2011, MNRAS, 414, 1715

Bonnerot, C., & Lu, W. 2019, arXiv e-prints, arXiv:1906.05865

Brown, T. M., Baliber, N., Bianco, F. B., et al. 2013, PASP, 125, 1031

Chambers, K. C., Magnier, E. A., Metcalfe, N., et al. 2016, arXiv e-prints, arXiv:1612.05560

Chevalier, R. A., & Irwin, C. M. 2011, ApJL, 729, L6

Coulter, D. A., Foley, R. J., Kilpatrick, C. D., et al. 2017, Science, 358, 1556

Dai, L., McKinney, J. C., Roth, N., Ramirez-Ruiz, E., & Miller, M. C. 2018, ApJL, 859, L20

Dessart, L., Ott, C. D., Burrows, A., Rosswog, S., & Livne, E. 2009, ApJ, 690, 1681

Dexter, J., & Kasen, D. 2013, ApJ, 772, 30

Drout, M. R., Chornock, R., Soderberg, A. M., et al. 2014, ApJ, 794, 23

Duncan, R. C., & Thompson, C. 1992, ApJL, 392, L9

Fernández, R., & Metzger, B. D. 2013, MNRAS, 435, 502

Foley, R. J., Jha, S. W., Pan, Y.-C., et al. 2016, MNRAS, 461, 433

Foley, R. J., McCully, C., Jha, S. W., et al. 2014, ApJ, 792, 29

Foley, R. J., Challis, P. J., Chornock, R., et al. 2013, ApJ, 767, 57

Fox, O. D., Johansson, J., Kasliwal, M., et al. 2016, ApJL, 816, L13

Gezari, S., Chornock, R., Rest, A., et al. 2012, Nature, 485, 217

Graham, M. J., Kulkarni, S. R., Bellm, E. C., et al. 2019, PASP, 131, 078001

Guillochon, J., & Ramirez-Ruiz, E. 2013, ApJ, 767, 25

Hansen, C. J., & Kawaler, S. D. 1994, Stellar Interiors. Physical Principles, Structure, and Evolution.

Ho, A. Y. Q., Phinney, E. S., Ravi, V., et al. 2019, ApJ, 871, 73

Ho, A. Y. Q., Perley, D. A., Kulkarni, S. R., et al. 2020, arXiv e-prints, arXiv:2003.01222

Holoien, T. W. S., Prieto, J. L., Bersier, D., et al. 2014, MNRAS, 445, 3263

Holoien, T. W.-S., Kochanek, C. S., Prieto, J. L., et al. 2016, MNRAS, 463, 3813

Karamehmetoglu, E., Fransson, C., Sollerman, J., et al. 2019, arXiv e-prints, arXiv:1910.06016

Kasen, D., & Bildsten, L. 2010, ApJ, 717, 245

Kashiyama, K., & Quataert, E. 2015, MNRAS, 451, 2656

Kasliwal, M. M., Kulkarni, S. R., Arcavi, I., et al. 2011, ApJ, 730, 134

Kasliwal, M. M., Kulkarni, S. R., Gal-Yam, A., et al. 2012, ApJ, 755, 161

Kuin, N. P. M., Wu, K., Oates, S., et al. 2019, MNRAS, 487, 2505

Lodato, G., King, A. R., & Pringle, J. E. 2009, MNRAS, 392, 332

Lorimer, D. R., Bailes, M., McLaughlin, M. A., Narkevic, D. J., & Crawford, F. 2007, Science, 318, 777

Lu, W., & Bonnerot, C. 2020, MNRAS, 492, 686

Lyutikov, M., & Toonen, S. 2019, MNRAS, 487, 5618

Margutti, R., Metzger, B. D., Chornock, R., et al. 2019, ApJ, 872, 18

Metzger, B. D., & Piro, A. L. 2014, MNRAS, 439, 3916

Metzger, B. D., Piro, A. L., & Quataert, E. 2008, MNRAS, 390, 781

Metzger, B. D., & Stone, N. C. 2016, MNRAS, 461, 948

Metzger, B. D., Martínez-Pinedo, G., Darbha, S., et al. 2010, MNRAS, 406, 2650

Miller, M. C. 2015, ApJ, 805, 83

Mockler, B., Guillochon, J., & Ramirez-Ruiz, E. 2019, ApJ, 872, 151

Ofek, E. O., Sullivan, M., Cenko, S. B., et al. 2013, Nature, 494, 65

Özel, F., Psaltis, D., Narayan, R., & McClintock, J. E. 2010, ApJ, 725, 1918

Perley, D. A., Mazzali, P. A., Yan, L., et al. 2019, MNRAS, 484, 1031

Piran, T., Svirski, G., Krolik, J., Cheng, R. M., & Shiokawa, H. 2015, ApJ, 806, 164

Prentice, S. J., Maguire, K., Smartt, S. J., et al. 2018, ApJL, 865, L3

Price, D. J., & Rosswog, S. 2006, Science, 312, 719

Proga, D., & Begelman, M. C. 2003a, ApJ, 582, 69

—. 2003b, ApJ, 592, 767

Quataert, E., Lecoanet, D., & Coughlin, E. R. 2019, MNRAS, 485, L83

Rau, A., Kulkarni, S. R., Ofek, E. O., & Yan, L. 2007, ApJ, 659, 1536

Rivera Sandoval, L. E., Maccarone, T. J., Corsi, A., et al. 2018, MNRAS, 480, L146

Roth, N., Kasen, D., Guillochon, J., & Ramirez-Ruiz, E. 2016, ApJ, 827, 3

Rybicki, G. B., & Lightman, A. P. 1986, Radiative Processes in Astrophysics, 400

Shappee, B. J., Prieto, J. L., Grupe, D., et al. 2014, ApJ, 788, 48

Shen, K. J., & Schwab, J. 2017, ApJ, 834, 180

Shen, R. F., Barniol Duran, R., Nakar, E., & Piran, T. 2015, MNRAS, 447, L60

Smith, N., Li, W., Foley, R. J., et al. 2007, ApJ, 666, 1116

Soker, N., Grichener, A., & Gilkis, A. 2019, MNRAS, 484, 4972

Strubbe, L. E., & Quataert, E. 2009, MNRAS, 400, 2070

Tartaglia, L., Sand, D. J., Valenti, S., et al. 2018, ApJ, 853, 62

Thornton, D., Stappers, B., Bailes, M., et al. 2013, Science, 341, 53

Tonry, J. L., Denneau, L., Heinze, A. N., et al. 2018, PASP, 130, 064505

Williams, S. C., Darnley, M. J., Bode, M. F., & Steele, I. A. 2015, ApJL, 805, L18

Zrake, J., & MacFadyen, A. I. 2013, ApJL, 769, L29